UCSB ATR-2 2017-1

Milestone: M3LW-17OR0402012

Summary of Progress on the ATR-2 Experiment Post-Irradiation Examination of Reactor Pressure Vessel Alloys

Prepared by

G. R. Odette, T. Yamamoto, P. B. Wells, N. Almirall,
K. Fields, D. Gragg
University of California, Santa Barbara

R. K. Nanstad, J. P. Robertson
Oak Ridge National Laboratory

K. Wilford, N. Riddle and T. Williams
Rolls-Royce

Document Completed: March 31, 2017

Prepared for
Dr. Keith Leonard (ORNL)
Dr. John Wagner (INL)
Dr. Richard Reister (DOE)

Disclaimer

This report was prepared as an account of work sponsored by an agency of the United States Government. Neither the United States Government nor any agency thereof, nor any of their employees, makes any warranty, express or implied, or assumes any legal liability or responsibility for the accuracy, completeness, or usefulness of any information, apparatus, product, or process disclosed, or represents that its use would not infringe privately owned rights. The above also applies to UCSB as an ORNL subcontractor. Reference herein to any specific commercial product, process, or service by trade name, trademark, manufacturer, or otherwise, does not necessarily constitute or imply its endorsement, recommendation, or favoring by the United States Government or any agency thereof. The views and opinions of authors expressed herein do not necessarily state or reflect those of the United States Government or any agency thereof.

Contents

List of Figures

List of Tables

Acknowledgements

We wish to acknowledge many individuals who have contributed to this work. First and foremost, the ATR-2 irradiation was made possible by the Nuclear Science User Facilities and the outstanding team of scientists, engineers and managers at the Idaho National Lab led by Michel Meyer, and including Michael Sprenger, Paul Murray, Joseph Nielson, Collin Knight, Thomas Maddock, Dan Ogden, James Cole, Todd Allen and Rory Kennedy. Other contributors include Keith Wilford and Tim Williams at Rolls Royce, Keith Leonard and Phil Edmondson at Oak Ridge National Lab, William Server at ATI consulting, Lynne Ecker and David Sprouster at Brookhaven National Lab, Timothy Hardin at EPRI, Grace Burke and Raymond Stofanak at BMPC and Naoki Soneda at CRIEPI. Rolls Royce provided the advanced steel matrix (ASM) for this experiment. The National Institute of Standards and Technology (NIST) provided the neutron research facilities to conduct the SANS studies and John Barker has contributed significantly in helping conduct these experiments. We would also like to acknowledge the Center for Advanced Energy Studies (CAES) Microscopy and Characterization Suite (MaCS) where the sample preparation for Atom Probe Tomography was completed, including Jatu Burns, Allyssa Bateman, and Joanna Taylor who significantly contributed to this process. Many other individuals at UCSB also contributed most notably Doug Klingensmith, Nicholas Cunningham and Yuan Wu. The work was financially supported by DOE through the NSUF, NEUP and LWRS Program (via ORNL).

Executive Summary

The UCSB ATR-2 irradiation experiment is designed to generate a new database on a wide variety of irradiated reactor pressure vessel (RPV) steels to fill a critical gap in predicting high fluence embrittlement for extended plant operation up to 80 years. The resulting database will serve as a foundation for the development of a physically based predictive model, that will address contribution to embrittlement from so-called, "late blooming" Mn-Ni-Si precipitate (MNSP) phases, which are not included in current regulatory models. Thus a major focus in this experiment is to characterize the effects of irradiation temperature, neutron flux and fluence, and alloy chemistry on MNSP evolution, and model how these features impact hardening and embrittlement, manifested as shifts in ductile-to-brittle transition temperature.

This report details the progress that has been made since July 1, 2016 in the UCSB ATR-2 post irradiation examination (PIE) program. A few highlights include:

- Atom probe tomography (APT) has been carried out on a number of surveillance steels, as well as a subset of alloys from the advanced steel matrix (ASM). These studies show that large volume fractions (f) of MNSPs can form even in low Cu steels at the high ATR fluence of $\approx 1.4 \times 10^{20}$ n/cm^2 and 290°C.
- The square root of MNSP f ($\sqrt{f}$) correlates well with the increases in yield stress ($\Delta\sigma_y$) with a relation that is well understood and modeled. This is illustrated in Figure 1 below for a large $\sqrt{f}$-$\Delta\sigma_y$ database that UCSB has assembled including the ATR-2 results. Likewise, empirically validated physical models can relate the $\Delta\sigma_y$ to shifts in the ductile to brittle fracture temperature (ΔT).
- The APT results show that the alloy Ni content plays a strong role in mediating the MNSP f as a function of neutron fluence.

- However at the ATR-2 fluence, which falls short of that needed for full precipitation, Cu also has a strong influence on f.
- The Advanced Steel Matrix (ASM) is intended to explore the possibility of developing higher Ni (3.5%) pressure vessel steels that have a number of attractive attributes, like higher unirradiated strength and toughness than conventional RPV steels. However, as noted above, in conventional steels f increases with Ni and, in Cu bearing steels, in some proportion to 2Ni + Cu. APT confirms the fact that an extremely high MNSP f form in 3.5% Ni advanced steels, but f decreases linearly with the alloy Mn content. This is due to the fact that precipitating a Ni atom requires approximately 1 (Si + Mn) atom to form MNSPs. Thus if the alloy is "Mn starved," more Ni stays in solution.
- A large number of Small Angle Neutron Scattering (SANS) and Small Angle X-ray Scattering (SAXS) measurements have also been carried out on the ATR-2 alloys. In conventional RPV steels, the MNSPs have SANS magnetic-to-nuclear scattering ratios (M/N) that are very similar to what would be expected for either the G or Γ_2 phases. In this case there is generally a reasonably good agreement between APT, SANS and SAXS f.
- However for alloys in the ASM that have low Mn contents, the precipitates have very high SANS M/N, which is consistent with the Ni_3Si phase as compositionally observed in APT. Thus the assumption of G or Γ_2 breaks down for both SANS and SAXS. Thus work is ongoing to allow a wider range of phase selection and to better quantify f by incorporating the actual APT measured precipitate compositions and combining SANS and SAXS measurements.

- Automated shear punch testing (SPT) has been completed on almost all alloys at UCSB. For the baseline condition, the automated SPT data correlates well with unirradiated tensile data, for example, with normal yield stress $\sigma_y = 1.78\tau_y$, where τ_y is the shear yield stress. The corresponding correlation for the irradiated condition is $\sigma_y = 2.06\tau_y$. This difference between the baseline and ATR-2 condition is thought to be due to the reduction in strain hardening caused by irradiation. SPT tests have been carried out on essentially all of the ATR-2 alloys at UCSB to estimate $\Delta\sigma_y$. All alloys provided to UCSB by ORNL will be subject to SPT in the future.
- Vickers microhardness measurements (μHv) have also been carried out on all paired unirradiated and ATR-2 irradiated alloys at UCSB.

Ongoing work includes comparing multiple techniques and optimizing ways to use data from different mechanical property testing and microstructural characterization techniques. Finally, a major focus of work through the rest of this fiscal year will be on completing SPT measurements on high fluence 290°C UCSB alloys and a large number of alloys in lower temperature (250 and 270°C) cups.

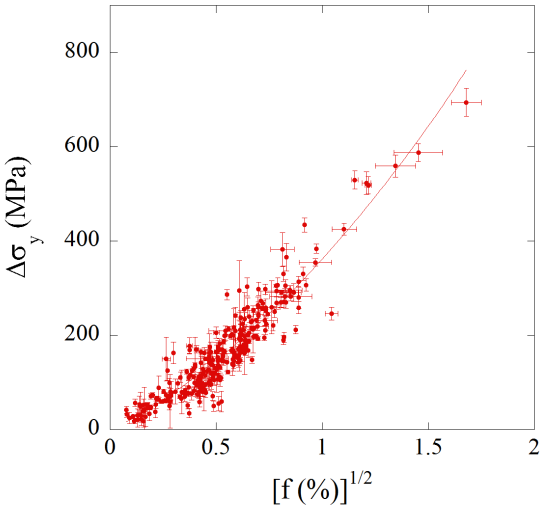

Figure 1 $\Delta\sigma_y$ vs $\sqrt{f}$ for the UCSB irradiated RPV steel database

1. Introduction

Here we describe continuation of work that was last summarized in "Update on the ATR–2 Reactor Pressure Vessel Steel High Fluence Irradiation Project," submitted on June 30, 2016 [1]. This report covers activities related to the ATR–2 irradiation experiment at the University of California, Santa Barbara for the period from July 1, 2016 to March 31, 2017. While the ultimate goal of this research is to create a new embrittlement prediction model for reactor pressure vessel (RPV) steels at high fluence and low flux, the focus to date has been on completing post irradiation examination (PIE) on the wide variety of RPV alloys included in the ATR-2 experiment. The major objective is to understand and model Cu-rich (CRPs) and especially MnNiSi-rich (MNSPs) precipitates, which form at high fluence, where the latter may cause significant unanticipated embrittlement that is currently unaccounted for in regulatory models.

1.1 Irradiation Conditions

The UCSB ATR-2 experiment reached a peak fluence of ≈ 1.4×10^{20} n/cm^2, which is about 40% higher than what most in service reactor pressure vessel (RPV) steels will reach at an 80 year extended life. In addition, four other capsules reached a peak fluence ranging from 5.1×10^{19} to 9.1×10^{19} n/cm^2. These capsules will be used to directly compare data from this experiment to lower fluence data, including what may be available in surveillance programs. The specimens were irradiated at four nominal temperatures: 250, 270, 290 and 310°C. The ≈ 109 cm long test train consisted of an assembly of concentric tubes, with an inner tube containing 13 thin-walled (0.125 mm) specimen cups.

The average flux, fluence and irradiation temperature (target and as run) for each cup are given in Table 1.1. Except for the two bottom and two top cups, the as-run temperatures

were very close to their target values. Details regarding determining the flux and temperature profiles in ATR-2 can be found in the INL as-run reports [2, 3].

To date the focus of all testing has been on samples from cups 7 and 8, which were at the highest fluence ≈ 13.8×10^{19} n/cm^2 and 292°C.

Table 1.1 Neutron flux, fluence (E > 1 MeV) and temperature for the various cups in the ATR-2 irradiation.

Cup	Flux (10^{12} n/cm^2-s)	Fluence (10^{19} n/cm2)	Target T_{irr} (°C)	Actual T_{irr} (°C)
1	1.34	5.11	290	247
2	1.94	7.43	290	268
3	2.54	10.35	290	280
4	3.13	11.90	270	268
5	3.36	12.80	250	255
6	3.58	13.70	290	285
7	3.64	13.90	290	291
8	3.60	13.70	290	293
9	3.47	13.20	290	293
10	3.21	12.30	310	319
11	2.89	11.05	290	292
12	2.17	9.08	290	264
13	1.52	5.79	290	238

1.2 RPV Steel Matrices

A number of different RPV steel matrices were included in the ATR-2 experiment, each with its own purpose. The sections below give a brief overview of a subset of these matrices, which were a focus of PIE over the past 9 months. This report almost entirely deals with PIE on disc multipurpose coupon specimens (DMC).

1.2.1 UCSB Matrix

The UCSB matrix includes 34 split-melt steels (SMS) with systematic variations in Cu, Ni and Mn contents to investigate the individual and combined effects of these solutes. The SMS were processed and have microstructures and properties that are typical of A-533B steels used for RPVs. The SMS include the L and CM series, based on their supplier. The L

and CM series are similar, but the CMs have a slightly larger base Mn content and a wider range of Ni. The compositions of the UCSB SMS alloys are shown in Table 1.2. In addition to the SMS, 11 simple model ferritic alloys variously containing only Cu, Ni, Mn, Si and Mo were also included in the experiment, though have not been examined.

Table 1.2 Composition of UCSB split melt steels included in the tensile matrix.

Alloy Code	Cu%	Ni%	Mn%	Cr%	Mo%	P%	C%	S%	Si%	Fe%
LA	0.40	0.00	1.37	0.06	0.54	0.005	0.14	0.005	0.22	97.26
LB	0.40	0.18	1.35	0.06	0.53	0.005	0.16	0.005	0.22	97.10
LC	0.41	0.86	1.44	0.06	0.55	0.005	0.14	0.008	0.23	96.30
LP	0.41	0.86	1.44	0.06	0.55	0.005	0.14	0.008	0.23	96.30
LD	0.38	1.25	1.38	0.070	0.53	0.005	0.19	0.015	0.23	96.02
LK	0.80	0.81	1.13	0.05	0.56	0.005	0.13	0.005	0.13	96.39
LJ	0.42	0.81	1.34	0.05	0.56	0.005	0.13	0.005	0.13	96.56
LG	0.01	0.74	1.37	0.05	0.55	0.005	0.16	0.005	0.22	96.90
LH	0.11	0.74	1.39	0.09	0.55	0.005	0.16	0.005	0.24	96.72
LI	0.20	0.74	1.37	0.09	0.55	0.005	0.16	0.005	0.24	96.65
LO	0.41	0.86	1.44	0.06	0.55	0.005	0.14	0.008	0.23	96.30
C1	0.01	0.01	1.67	0.04	0.56	0.003	0.13	0.004	0.15	97.42
C2	0.01	0.01	1.65	0.04	0.56	0.041	0.14	0.004	0.16	97.39
C3	0.02	0.85	1.60	0.00	0.49	0.006	0.13	0.000	0.16	96.74
C4	0.02	0.86	1.53	0.05	0.55	0.031	0.16	0.003	0.16	96.64
C5	0.02	0.86	1.61	0.04	0.53	0.050	0.15	0.000	0.16	96.58
C6	0.02	1.68	1.50	0.05	0.54	0.007	0.15	0.003	0.17	95.88
C7	0.00	1.70	1.55	0.05	0.56	0.047	0.16	0.003	0.17	95.76
C8	0.01	0.86	0.01	0.04	0.55	0.004	0.13	0.002	0.14	98.25
C9	0.01	0.86	0.85	0.04	0.55	0.003	0.15	0.003	0.15	97.38
C10	0.02	0.88	1.66	0.05	0.53	0.008	0.16	0.004	0.17	96.52
C11	0.34	0.85	1.64	0.02	0.53	0.006	0.15	0.003	0.18	96.28
C12	0.86	0.84	1.65	0.02	0.51	0.006	0.15	0.003	0.17	95.79
C13	0.11	0.83	1.61	0.00	0.51	0.004	0.15	0.000	0.16	96.63
C14	0.11	0.83	1.62	0.00	0.52	0.040	0.16	0.000	0.17	96.55
C15	0.22	0.02	1.59	0.02	0.58	0.002	0.14	0.003	0.15	97.28
C16	0.22	0.82	1.58	0.00	0.51	0.004	0.16	0.000	0.25	96.46
C17	0.22	1.59	1.54	0.00	0.50	0.004	0.16	0.000	0.25	95.74
C18	0.43	0.02	1.70	0.02	0.56	0.002	0.14	0.003	0.15	96.98
C19	0.42	0.85	1.63	0.01	0.51	0.005	0.16	0.003	0.16	96.25
C20	0.43	1.69	1.63	0.02	0.50	0.006	0.16	0.003	0.16	95.40
C21	0.42	0.84	0.01	0.02	0.58	0.002	0.14	0.003	0.14	97.85
C22	0.42	0.84	0.84	0.02	0.56	0.002	0.14	0.003	0.14	97.04
C31	0.01	0.80	1.65	0.05	0.51	0.006	0.16	0.003	0.17	96.64

1.2.2 Surveillance and Program Alloy Matrix

Nine surveillance alloys were procured specifically for the ATR-2 experiment. In addition, eleven other archival surveillance alloys, which had mostly been previously studied by UCSB in the Irradiation Variables Program (IVAR), were also included. While flux effects have been extensively studied for many years, they are still not fully understood. Thus, the surveillance alloys will allow for direct comparison of results from the ATR-2 intermediate-flux test reactor irradiation with those from the much lower flux surveillance irradiations. The compositions of the surveillance alloys are given in Table 1.3. Note the 9 new surveillance alloys are not identified by the plant specific vessel code.

Table 1.3 Composition (wt.%) of surveillance and program alloys.

Alloy	Cu%	Ni%	Mn%	Cr%	Mo%	P%	C%	S%	Si%	Fe%
SB1*	0.20	0.60	1.33	0.11	0.49	0.005	0.22	0.016	0.23	96.82
SB2*	0.06	0.75	0.79	0.35	0.58	0.010	0.20	0.009	0.28	96.97
SB3*	0.05	0.56	1.32	0.08	0.59	0.010	0.24	0.016	0.24	96.89
SW1*	0.14	0.19	1.06	0.06	0.50	0.016	0.13	0.009	0.27	95.90
SW2*	0.36	0.78	1.42	0.04	0.49	0.013	0.18	0.011	0.18	96.54
SW3*	0.22	0.72	1.37	0.09	0.48	0.016	0.12	0.011	0.20	96.77
SW4*	0.03	0.90	0.94	0.03	0.23	0.004	0.14	0.014	0.32	97.39
SW5*	0.04	0.95	1.41	0.13	0.48	0.009	0.09	0.009	0.45	96.44
SW6*	0.29	0.60	1.44	0.14	0.36	0.014	0.10	0.011	0.50	96.55
QC1	0.24	0.54	1.70	0.06	0.43	0.014	0.09	0.016	0.56	96.35
QC2	0.24	0.56	1.68	0.07	0.40	0.014	0.09	0.016	0.55	96.38
D3	0.28	0.63	1.59	0.08	0.43	0.011	0.09	0.015	0.51	96.36
HB	0.22	0.07	1.37	0.16	0.46	0.014	0.13	0.016	0.29	97.27
MP	0.19	1.02	1.30	0.05	0.51	0.017	0.11	0.015	0.18	96.61
TW	0.15	0.08	1.61	0.15	0.49	0.019	0.12	0.014	0.28	97.09
WA	0.21	0.63	1.69	0.14	0.40	0.014	0.08	0.013	0.45	96.37
WB	0.28	0.69	1.63	0.10	0.40	0.018	0.09	0.009	0.54	96.52
WC	0.06	0.62	1.30	0.08	0.31	0.009	0.08	0.010	0.37	97.22
W62	0.23	0.60	1.61	0.12	0.39	0.016	0.08	0.007	0.59	96.59
W63	0.3	0.69	1.65	0.10	0.43	0.016	0.10	0.011	0.63	96.37
W65	0.22	0.60	1.45	0.09	0.39	0.015	0.08	0.015	0.48	96.88
W67	0.18	0.61	1.27	0.14	0.43	0.009	0.10	0.009	0.50	97.99
EC**	0.35	0.60	1.30	0.04	0.44	0.005	0.16	0.009	0.17	96.93
ED**	0.40	0.60	1.36	0.04	0.44	0.006	0.12	0.013	0.51	96.51
FE**	0.01	1.69	1.30	0.02	0.51	0.009	0.21	0.006	0.20	96.05

**Procured by ORNL and ATI Consulting*
***Program alloy*

1.2.3 Advanced Steel Matrix (ASM)

RPV steels in US light water reactors (LWR) have typical alloy compositions (wt.%) ranging from ≈ .02 to 0.4Cu, 0.2 to 1.0Ni, 1.0 to 1.8 Mn, and 0.1 to 0.5 Si. Rolls Royce (RR) supplied a new advanced steel matrix (ASM) to the ATR-2 experiment with a much wider range of solute contents than in typical US RPV steels. The purpose of this matrix is twofold. First, the wide range of compositions in these alloys will improve the understanding of the synergistic relationships among the various solutes. Second, this matrix will assist in the development of new alloys for future light water reactors. High Ni steels have a number of attractive attributes, like higher unirradiated strength and toughness than conventional RPV steels, but are potentially more susceptible to irradiation embrittlement due to the strong correlation between alloy Ni content and MNSP formation. The key question is whether this effect will still be observed if the alloy Mn and/or Si are significantly reduced. Figure 1.1 shows the ranges of compositions explored in previous UCSB irradiations (blue box) and the ATR-2 irradiation (red box) due to the addition of the ASM (blue points).

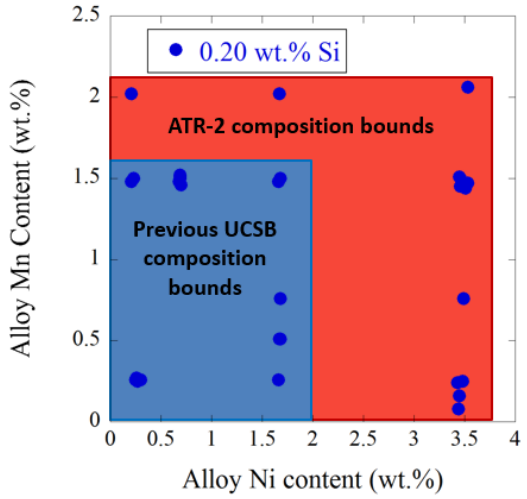

Figure 1.1. Range of Mn and Ni contents for all ASM alloys with 0.20 wt.% Si (blue dots), along with boxes showing the range of compositions explored in previous UCSB irradiations (blue box) and the in ATR-2 irradiation (red box).

Table 1.4 Composition (wt.%) of Advanced Steel Matrix alloys.

Alloy	Cu%	Ni%	Mn%	Cr%	Mo%	P%	C%	Si%	Fe%
R1	0.06	0.30	0.26	0.10	0.49	0.005	0.21	0.21	98.37
R2	0.06	0.27	0.25	0.11	0.49	0.006	0.15	0.20	98.46
R3	0.06	0.27	0.25	0.10	0.52	0.004	0.07	0.20	98.53
R4	0.06	0.26	0.26	0.11	0.53	0.006	0.20	0.62	97.95
R5	0.06	0.27	0.25	0.10	0.52	0.005	0.20	0.05	98.55
R6	0.20	0.25	0.26	0.10	0.52	0.006	0.20	0.22	98.24
R7	0.58	0.25	0.25	0.10	0.53	0.005	0.23	0.20	97.86
R8	0.06	0.25	0.26	0.10	0.52	0.035	0.21	0.20	98.37
R9	0.58	0.25	0.26	0.10	0.52	0.033	0.21	0.21	97.84
R10	0.06	3.53	1.47	0.10	0.48	0.008	0.27	0.22	93.86
R11	0.06	3.49	1.46	0.10	0.52	0.005	0.16	0.20	94.01
R12	0.06	3.51	1.44	0.10	0.52	0.005	0.05	0.20	94.12
R13	0.07	3.49	1.48	0.10	0.52	0.005	0.23	0.63	93.48
R14	0.06	3.44	1.48	0.10	0.52	0.006	0.22	0.03	94.14
R15	0.31	3.47	1.48	0.10	0.52	0.008	0.21	0.20	93.70
R16	0.60	3.46	1.50	0.10	0.52	0.004	0.22	0.20	93.40
R17	0.06	3.45	1.51	0.10	0.50	0.029	0.23	0.20	93.92
R18	0.59	3.44	1.50	0.10	0.50	0.029	0.21	0.20	93.43
R19	0.06	1.66	0.26	0.13	0.52	0.008	0.23	0.20	96.93
R20	0.06	1.66	0.26	0.10	0.52	0.005	0.07	0.20	97.13
R21	0.06	1.66	0.26	0.10	0.52	0.005	0.23	0.05	97.12
R22	0.06	1.68	1.50	0.10	0.52	0.006	0.29	0.21	95.63
R23	0.06	1.66	1.48	0.10	0.50	0.006	0.06	0.21	95.92
R24	0.06	1.71	1.51	0.10	0.50	0.005	0.26	0.59	95.27
R25	0.06	1.68	1.50	0.10	0.50	0.004	0.05	0.63	95.48
R26	0.05	3.48	0.25	0.10	0.52	0.009	0.26	0.19	95.14
R27	0.06	3.43	0.24	0.10	0.52	0.003	0.06	0.20	95.39
R28	0.06	3.47	0.25	0.10	0.52	0.006	0.27	0.62	94.70
R29	0.06	3.48	0.26	0.10	0.52	0.004	0.05	0.62	94.91
R30	0.06	0.21	2.02	0.10	0.52	0.004	0.19	0.20	96.70
R31	0.06	1.67	2.02	0.10	0.53	0.005	0.21	0.20	95.21
R32	0.06	3.53	2.06	0.13	0.53	0.010	0.22	0.23	93.23
R33	0.06	3.45	0.16	0.10	0.52	0.005	0.22	0.20	95.29
R34	0.07	3.44	0.08	0.09	0.52	0.006	0.22	0.19	95.38
R35	0.06	0.23	1.50	0.11	0.49	0.007	0.27	0.21	97.12
R36	0.06	0.23	1.50	0.11	0.49	0.007	0.27	0.21	97.12
R37	0.06	0.21	1.48	0.10	0.52	0.005	0.06	0.21	97.36
R38	0.06	0.21	1.49	0.10	0.52	0.007	0.27	0.62	96.72
R39	0.06	0.21	1.48	0.10	0.52	0.003	0.05	0.59	96.99
R40	0.04	0.70	1.46	0.11	0.49	0.004	0.21	0.21	96.78
R41	0.12	0.69	1.52	0.10	0.52	0.005	0.20	0.20	96.65
R42	0.04	0.69	1.50	0.10	0.52	0.015	0.20	0.21	96.73
R43	0.08	0.68	1.48	0.10	0.52	0.017	0.23	0.19	96.70
R44	0.13	0.69	1.51	0.10	0.52	0.021	0.21	0.21	96.61
R45	0.06	0.26	0.27	2.28	0.52	0.003	0.21	0.20	96.20
R46	0.06	3.46	1.45	2.34	0.52	0.006	0.21	0.20	91.75
R47	0.06	1.68	0.76	0.10	0.50	0.005	0.28	0.21	96.41
R48	0.07	3.49	0.76	0.10	0.50	0.003	0.28	0.21	94.59
R49	0.06	1.67	0.51	1.21	0.50	0.005	0.22	0.20	95.63
R50	0.06	1.68	0.51	2.32	0.51	0.003	0.23	0.20	94.49

1.3 Characterization Techniques

Background and experimental details of the microstructure characterization techniques employed in this PIE program are described in [1], including atom probe tomography, small angle neutron scattering and small angle x-ray scattering. In addition, this previous report gives an overview on shear punch testing (SPT) using a one test at a time manual SPT punch and die tool. Since then a major focus has been on completing an "automated" SPT instrument, which has undergone full qualification prior to application to the irradiated ASM alloys. The automated SPT apparatus is described in the next section, followed by a brief summary of the microhardness testing method.

1.3.1 Automated SPT

The single punch manual SPT punch and die previously used in this PIE campaign requires a standard load frame to apply force to the punch. Manual single punch tests are time consuming and may result in higher radiation exposures to the test personnel from activated steel samples due to the time and handling required. To address these issues, we developed an automated SPT instrument. The instrument consists of a pneumatically clamped upper assembly, with a hydraulic actuator and a load sensor. A precision punch is coupled to the load sensor through a hardened guide for accurate alignment. Both the guide and punch are interchangeable so different SPT coupon specimen diameters can be used. The lower assembly consists of an indexing loading table that supports and positions the disc multipurpose coupon (DMC) for testing. The loading table can be removed and exchanged to allow varying diameter test coupons, though the focus to date has been on designing the instrument to test the 20 mm DMCs. The current design allows up to ten 3.0 mm punch diameter SPTs per 20 mm coupon; however the SPT can easily be modified to obtain a larger number of tests per DMC.

A precision die placed under the test specimen that is exactly matched to the punch for optimal clearance. A spring-loaded follower contacts the bottom face of the test specimens and tracks the corresponding deflection throughout the punching process. The load cell and deflection sensor provide the load-displacement data to compute shear stress and strain. The SPT tool is computer-controlled (clamping, load actuation and digital data acquisition).

The main benefit of the automated instrument, shown in Figure 1.2, is a much higher testing throughput relative to the single punch manual fixture. Another advantage is that the automated SPT instrument is self-contained, occupying a relatively small footprint, and does not require a load frame. Further, automated SPT reduces radiation exposures. Testing on the entire Advanced Steel Matrix in the baseline condition has recently been completed to determine the "optimal" offset to use when determining the shear yield, as discussed further section 2.3. The results from the automated SPT instrument and data reduction procedure compare very favorably with the previous manual tester.

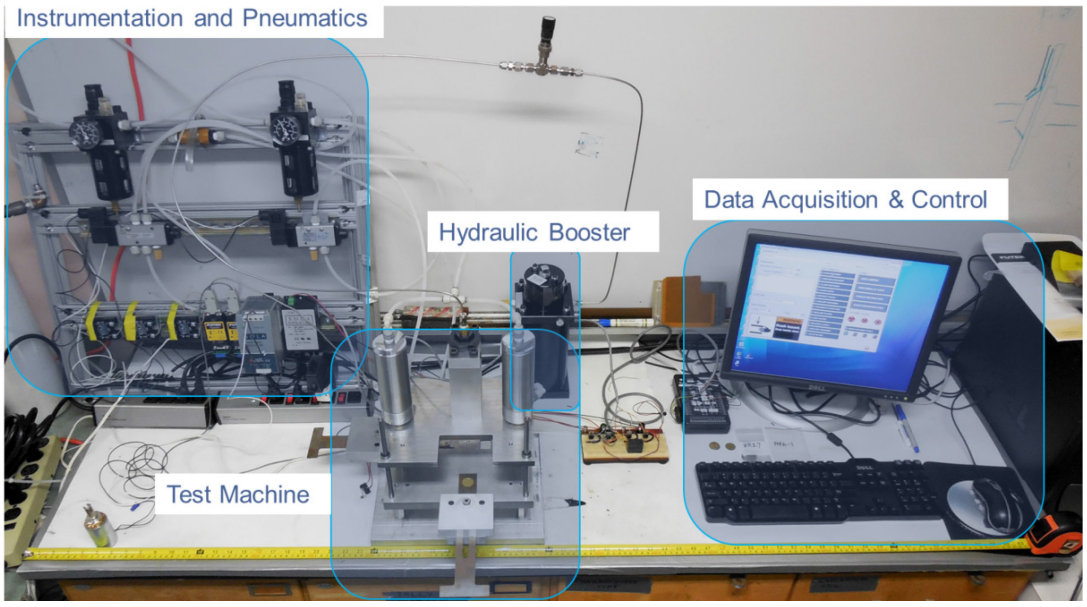

Figure 1.2. The automated SPT instrument.

1.3.2 Microhardness Testing

Vickers microhardness (μH_v) testing was carried out at UCSB on the ASM matrix. All μH_v measurements were performed on a LECO 400 series microhardness tester with digitized image analysis. A square-base diamond-pyramid indenter was used with a 500g load and a 10 second dwell time. Both diagonal lengths of the indents were measured and the average value of the two was used to determine the microhardness. Prior to each test series the system is recalibrated/validated by measuring five indents on a certified hardness calibration block. Changes in μH_v were used to estimate the corresponding changes in yield stress ($\Delta\sigma_y$) based on a nominal relation, $\Delta\sigma_y$ (MPa) = 3.33*$\Delta\mu H_v$ (kg/mm^2).

Seven 3 mm discs were loaded into multi-specimen holders and polished using 600 and 1200 grit followed by fine polishing on a vibromet with 0.3 μm alumina in an ethelyne glycol solution to produce a mirror surface finish. Ten automated indents were made on each 3 mm disc. The spacing between indents was at minimum 2.5 times the indent diagonal, in order to avoid the previously plastically deformed region. The indents diameters were read off a digital image with a camera coupled to a 40x viewing scope. If the difference between two indent diagonal lengths was greater than 5.0%, the data was discarded. The average and standard deviation for the indents were calculated for each alloy/condition and the standard error was determined by S.E. = S.D./√n. The S.E. was used as the uncertainty for the measurement of a given condition. The uncertainty for the $\Delta\mu H_v$ was determined using a root-sum-square of the uncertainties from both the baseline and irradiated conditions.

1.4 Status of Characterization and Testing

The progress made since the previous report [1] is described in the following two sections.

1.4.1 Microstructural Characterization

Precipitation in the irradiated alloys was characterized using multiple techniques. Of the 139 alloys in cups 7 and 8 (excluding CRIEPI and UCSB model alloys), 33 have been characterized by APT, 37 by SANS, 90 by SAXS and 43 by XRD. SANS beamtime is currently scheduled at the NIST Center for Neutron Research in early May to carry out SANS on 20 additional alloys from cups 7 and 8. Additional APT on alloys in cups 7 and 8 is being planned.

1.4.2 Mechanical Property Testing

Baseline condition automated SPT has been carried out on almost all of alloys alloy in the ATR-2 matrix. A corresponding total of 85 SPT on irradiated alloys have been carried out, and the remaining 18 DMC currently at UCSB are scheduled to be tested in April 2017. A number of alloys, which are still in LAMDA or ORNL hot cells, will be sent to UCSB for SPT at a later date. Note that some alloys at ORNL are a lower priority and are not currently targeted for testing. Table 1.5 summarizes the current status of SPT. Note again, the number of alloys in Cups 7 and 8 do not include the CRIEPI steels and UCSB model alloy matrices.

Table 1.5 Status of automated shear punch testing for cups 7 and 8.

Technique	# of Alloys in Cups 7/8	Alloys at UCSB	Tested	To be Tested	At ORNL
SPT	139	102	85	17	26

Microhardness testing was completed on the entire ASM baseline matrix and all corresponding irradiated Cup 8 alloys currently at UCSB (48). Note, there are 6 additional heat-treated steels in the advanced alloy matrix but these results have not been fully analyzed.

2. Results and Preliminary Analysis

2.1 Atom Probe Tomography

This section focuses on the results and analysis of microstructural characterization of a subset of the alloys in cups 7 and 8. During this period we focused on the effect of Ni and Mn on precipitation in the ASM alloys and also on characterizing the surveillance steels, including the 9 new welds and base metals. A few program alloys were also characterized. Ultimately this microstructural data will allow us to characterize the effect of a wide range of flux, fluence and alloy composition on the volume fraction (f), number density (N), average size (<d>), composition and character of precipitates. We also compare the results of SANS and APT measurements.

2.1.1 Surveillance and Program Steels

Figure 2.1 shows an example of APT solute maps for the high Cu, medium Ni weld SW6 (0.30% Cu, 0.60Ni, 1.30Mn, 0.50Si in weight %). APT found $f \approx 0.67\%$ of 2-3 nm Cu-Ni-Mn-Si precipitates.

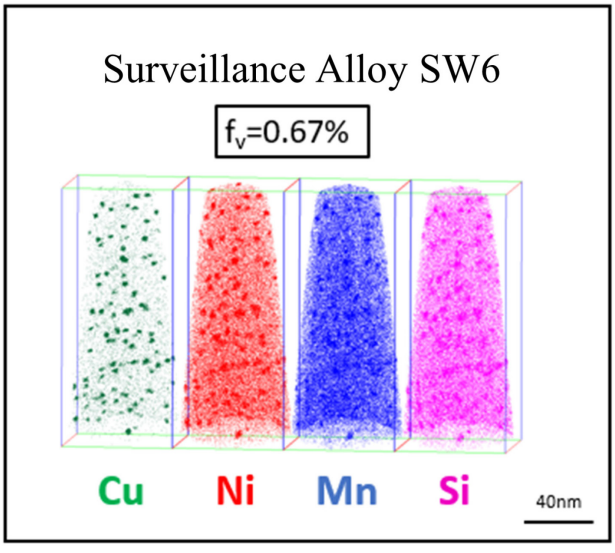

Figure 2.1. APT solute maps for a high 0.30Cu, intermediate 0.60Ni, 1.30Mn, 0.50Si surveillance weld (SW6) with a large precipitate $f \approx 0.67$.

Figure 2.2 shows solute maps and f for the program alloy FE with 0.01% Cu, 1.70% Ni, 1.30% Mn, 0.20% Si demonstrating that MNSPs form even in the absence of a significant amount of Cu at high fluence, especially at high Ni.

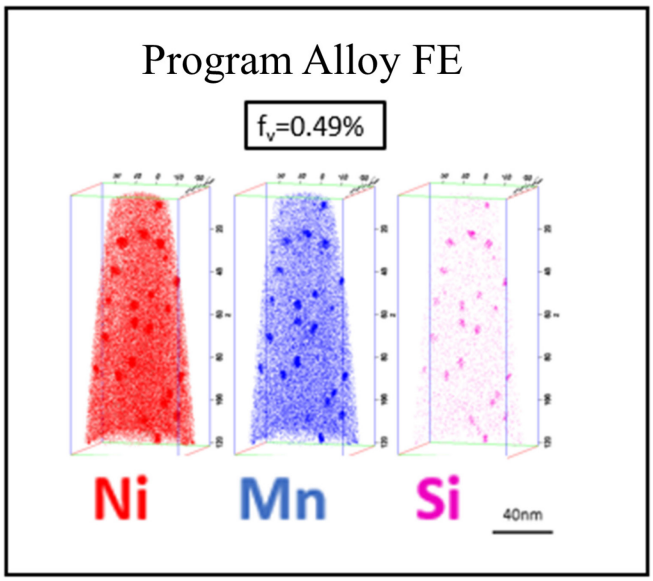

Figure 2.2. APT solute maps for an irradiated low 0.01Cu, high 1.70Ni, 1.30Mn, 0.20Si program plate (FE) with f ≈ 0.49%

Ongoing APT analysis includes the mapping of precipitate size distributions, quantifying segregation of Cu-Ni-Mn-Si-P and examining precipitate nucleation on dislocations and loops that are made visible by their solute atmospheres. For example, Figure 2.3 shows APT solute maps of Mn-Ni-Si in a low (0.04% Cu), medium-high (0.95% Ni) surveillance weld, SW5. Segregation of the solutes, especially Si, to what appears to be a helical dislocation and perhaps another dislocation segment are obvious. Precipitates form in the segregated regions. These associations are more clearly shown by the 4% Si isoconcentration surfaces. The compositions of the precipitates on dislocations are similar to those in the matrix. A general observation is that MNSPs in low Cu and medium Ni steels predominantly heterogeneously nucleate on dislocations, loops and grain boundaries. Indeed, matrix MNSP may nucleate on small loops and envelope them during growth. Future work

includes S/TEM mapping of precipitate-dislocation interactions, as well as measuring dislocation loop densities and quantifying solute segregation at various microstructural features. These results will inform the advanced thermo-kinetic models of MNSP precipitation being developed in our collaboration with Professor Dane Morgan's group at the University of Wisconsin.

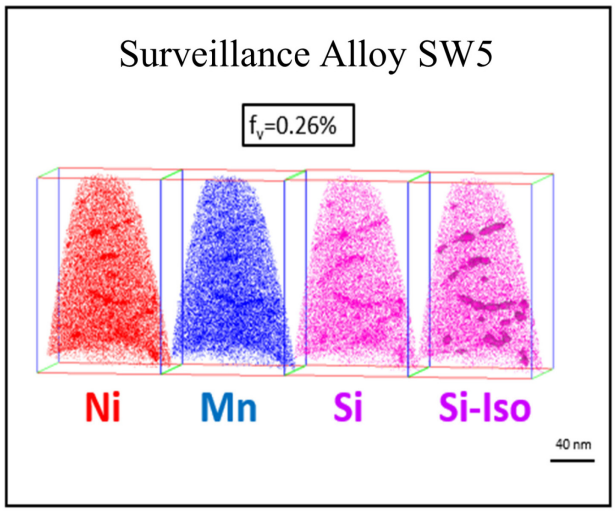

Figure 2.3. APT solute maps for an irradiated low 0.04Cu, medium-high 0.95Ni, 1.40Mn, 0.45Si surveillance weld (SW5) showing solute segregation and precipitation on dislocations with f ≈ 0.26%.

A summary of APT compositions for the 9 new surveillance and 3 program alloys is shown in Table 2.1. This table shows that all alloys with bulk Cu > 0.15 at.% form precipitates rich in Cu (15-35% Cu) and deplete the matrix Cu to ≈ 0.06-0.07%. This is consistent with previous studies that show that well defined Cu precipitates (CRPs) will form only at Cu levels ≥ 0.07% [4]. Though CRPs may not form, Cu still has a catalyzing effect for formation of MNSPs even at levels < 0.07%. Table 2.2 shows the precipitate <d>, N and f for the surveillance alloys. Figure 2.4 shows the APT f as a function of the alloy bulk Cu content for the surveillance and program alloys. Increased Cu leads to significantly increased precipitate f at typical Ni contents of 0.5 – 1.0 at.%, but this effect is decreases at lower Ni contents (0 – 0.49 at.%).

Table 2.1. APT bulk, matrix and precipitate compositions for 9 surveillance alloys and 3 program alloys in the cup 7 irradiated condition.

Alloy	Bulk				Matrix				Precipitate			
	Cu	Ni	Mn	Si	Cu	Ni	Mn	Si	Cu	Ni	Mn	Si
SW1	0.15	0.13	0.86	0.40	0.06	0.10	0.82	0.35	35.0	15.4	30.0	19.6
SB1	0.16	0.59	0.87	0.55	0.06	0.42	0.78	0.45	21.4	35.7	20.4	22.4
SB2	0.04	0.61	0.55	0.51	0.04	0.55	0.54	0.46	2.0	46.8	12.3	38.9
SW2	0.19	0.78	1.09	0.37	0.06	0.50	0.94	0.26	20.9	36.7	25.0	17.5
SB3	0.04	0.47	0.88	0.51	0.04	0.39	0.84	0.44	1.4	38.9	22.1	37.7
SW3	0.27	0.70	0.90	0.40	0.06	0.46	0.75	0.28	28.0	33.6	21.4	17.0
SW4	0.03	0.92	0.99	0.94	0.03	0.77	0.93	0.82	0.6	44.0	19.5	35.9
SW5	0.03	0.79	1.06	0.79	0.03	0.68	1.02	0.71	0.4	44.9	18.2	36.5
SW6	0.23	0.58	1.19	0.92	0.07	0.39	1.06	0.77	25.0	29.1	21.7	24.2
EC*	0.25	0.61	0.97	0.36	0.04	0.44	0.85	0.27	23.2	33.5	26.5	16.8
ED*	0.25	0.50	1.02	1.03	0.06	0.36	0.91	0.87	15.4	27.9	23.2	33.4
FE*	0.00	1.70	1.02	0.08	0.00	1.48	0.90	0.06	0.1	60.3	32.0	7.7

**Program Alloy*

Table 2.2 APT precipitate <d>, N and f for 9 surveillance and 3 program alloys.

Alloy	APT Bulk Composition				<d>	+/-	N	+/-	f	+/-
	Cu	Ni	Mn	Si	(nm)	(nm)	(10^{23} m^{-3})	(10^{23} m^{-3})	(%)	(%)
SW1	0.15	0.13	0.86	0.40	2.94	0.20	1.90	0.51	0.25	0.03
SB1	0.16	0.59	0.87	0.55	2.95	0.02	3.88	1.00	0.49	0.05
SB2	0.04	0.61	0.55	0.51	2.32	0.16	1.95	0.31	0.14	0.07
SW2	0.19	0.78	1.09	0.37	3.32	0.20	3.64	0.86	0.66	0.14
SB3	0.04	0.47	0.88	0.51	2.60	0.52	8.02	0.50	0.21	0.15
SW3	0.27	0.70	0.90	0.40	3.11	0.21	4.11	0.61	0.75	0.05
SW4	0.03	0.92	0.99	0.94	2.50	0.08	3.78	0.40	0.37	0.04
SW5	0.03	0.79	1.06	0.79	2.40	0.07	3.18	0.51	0.25	0.03
SW6	0.23	0.58	1.19	0.92	2.83	0.05	5.73	0.15	0.67	0.01
EC*	0.25	0.61	0.97	0.36	3.02	0.22	3.78	0.18	0.53	0.08
ED*	0.25	0.50	1.02	1.03	2.88	0.35	3.38	0.28	0.53	0.03
FE*	0.00	1.70	1.02	0.08	3.26	0.50	2.59	0.60	0.39	0.11

** Program Alloy*

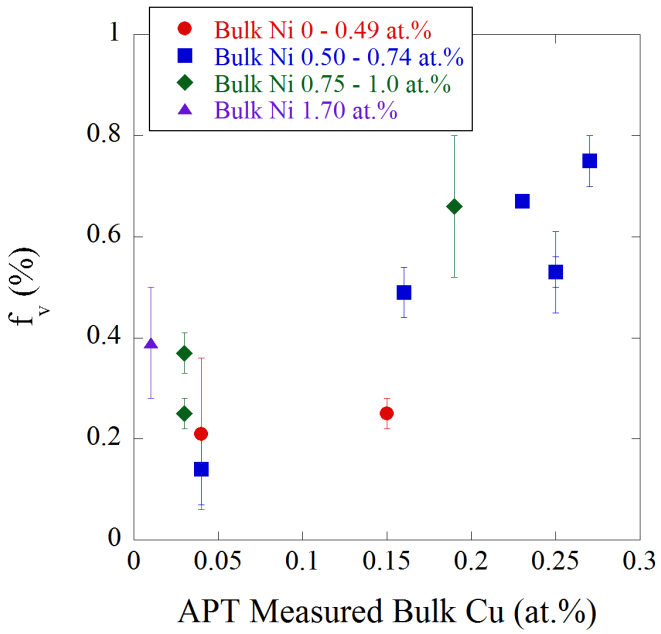

Figure 2.4. APT f versus the measured bulk Cu content (at.%) for the surveillance and program alloys showing the strong effect of both Cu and Ni.

2.1.2 Advanced Steel Matrix

Atom probe tomography has been completed on 9 alloys from the ASM with systematic variations in bulk Ni and Mn contents at low Cu (< 0.06 at.%). A summary of this data is shown in Table 2.3 and Table 2.4.

Table 2.3 APT bulk, matrix and precipitate compositions for 9 ASM alloys in cup 8.

Alloy	Bulk				Matrix				Precipitate			
	Cu	Ni	Mn	Si	Cu	Ni	Mn	Si	Cu	Ni	Mn	Si
R1	0.05	0.24	0.24	0.49	0.04	0.21	0.22	0.44	1.5	37.1	14.6	46.8
R17	0.04	3.50	1.04	0.44	0.02	2.15	0.51	0.15	0.9	62.8	23.9	12.5
R19	0.05	1.80	0.24	0.47	0.05	1.55	0.22	0.35	1.0	64.4	5.1	29.4
R22	0.05	1.62	1.23	0.46	0.04	1.25	1.06	0.33	0.8	54.1	26.5	18.6
R26	0.04	3.40	0.22	0.39	0.04	2.91	0.19	0.25	0.9	73.5	4.7	20.8
R34	0.06	3.39	0.06	0.40	0.05	3.09	0.06	0.31	0.9	75.9	1.2	22.0
R35	0.04	0.19	1.34	0.46	0.04	0.17	1.27	0.44	1.3	26.4	42.4	30.0
R39	0.03	0.75	0.80	0.46	0.03	0.63	0.75	0.37	0.8	46.8	19.7	32.7
R48	0.05	3.45	0.48	0.42	0.04	2.58	0.32	0.19	1.0	69.2	12.5	17.2

Table 2.4 APT precipitate <d>, N and f for 9 ASM alloys in cup 8.

Alloy	APT Bulk Composition				<d>	+/-	N	+/-	f	+/-
	Cu	Ni	Mn	Si	(nm)	(nm)	(10^{23} m^{-3})	(10^{23} m^{-3})	(%)	(%)
R1	0.05	0.24	0.24	0.49	2.31	0.02	0.92	0.40	0.08	0.15
R17	0.04	3.50	1.04	0.44	2.58	0.09	22.2	0.12	2.44	0.17
R19	0.05	1.80	0.24	0.47	2.47	0.03	5.07	0.09	0.42	0.04
R22	0.05	1.62	1.23	0.46	2.15	0.08	13.4	0.15	0.89	0.12
R26	0.04	3.40	0.22	0.39	2.46	0.04	8.37	1.69	0.69	0.11
R34	0.06	3.39	0.06	0.40	2.17	0.10	6.53	2.05	0.44	0.10
R35	0.04	0.19	1.34	0.46	2.22	0.03	1.83	0.27	0.11	0.08
R39	0.03	0.75	0.80	0.46	2.60	0.13	2.42	0.40	0.29	0.04
R48	0.05	3.45	0.48	0.42	2.29	0.08	21.2	0.60	1.41	0.22

2.1.2.1 Effects of Ni and Mn in Low Cu Steels

Figure 2.5 to Figure 2.7 show the effect of Ni and Mn on precipitation of MNSPs. Solute maps for four low Cu (< 0.07%) steels with varying Ni contents from 0.3 to 3.5% are shown in Figure 2.5. These alloys all nominally contained 0.04 – 0.06 wt.% Cu, 1.46 – 1.51 wt.% Mn, 0.20 – 0.21 wt.% Si. APT finds 2-3 nm diameter MNSPs with number densities of 10^{23}-10^{24} m^{-3}. There is a strong correlation between bulk Ni content of the alloys and the MNSP f, that increases from 0.08% in the low 0.3Ni steel to 2.44% in the highest 3.50Ni steel. These results are consistent with previous observations of the dominant role of Ni on significant precipitation at very high ϕt, even in low Cu steels [5].

Note that in the case of 0.8 wt.% Ni alloy most precipitates are located on dislocations and grain boundaries. Mn, Ni and Si all segregate to these microstructural features, especially Si. It is known that Cu precipitates catalyze the initial formation of MNSPs. In the effective absence of Cu, and at lower bulk Ni, the precipitates have difficulty nucleating homogeneously in the defect free matrix. Thus microstructural features such as dislocations, loops and grain boundaries act as heterogeneous nucleation sites for MNSPs. Such precipitate-dislocation associations were also observed in the ATR-2 surveillance steels.

Note that several tips for the 0.3 wt.% Ni datasets have precipitates on dislocations enriched in Si (not shown here). However, due to the small sampling volumes of APT, these features are not present in every dataset.

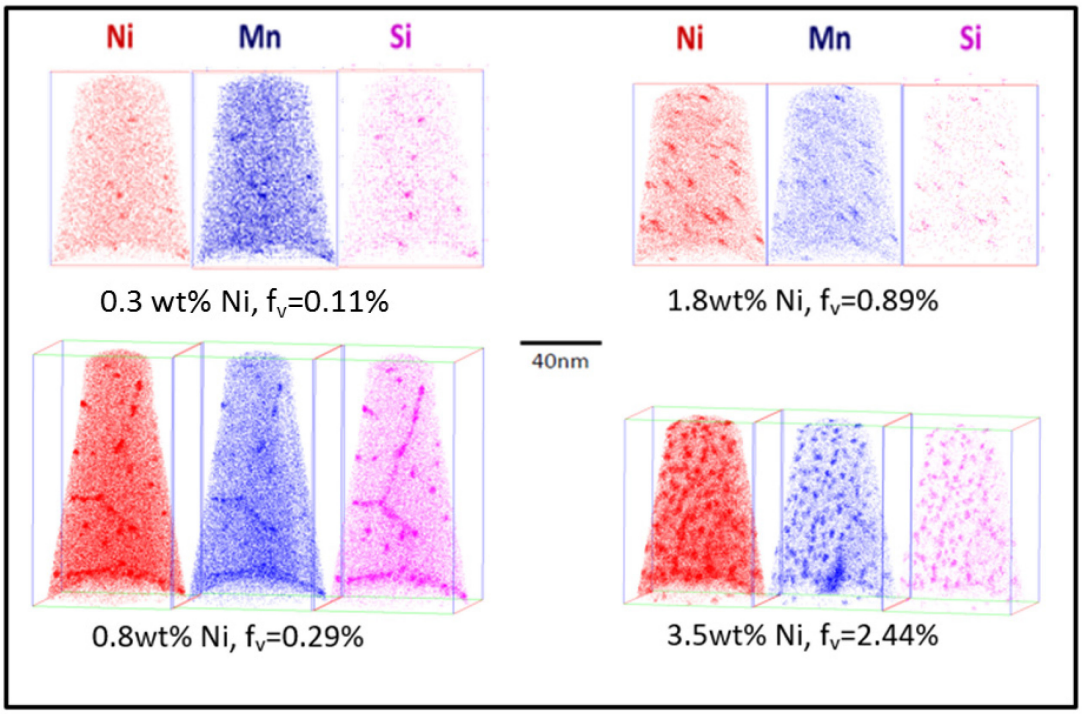

Figure 2.5. Solute maps for the irradiated ASM alloys with varying Ni contents from 0.30-3.50 wt.% Ni. The nominal bulk contents of the other solutes are ≈ 0.05Cu, 1.50Mn, 0.20Si.

The average precipitate <d> and N for are shown in Figure 2.6 for a series of low Cu ASM alloys with varying Ni and Mn contents. With the exception of the very low Ni steels, the <d> are generally similar (<d>≈ 2.36 ± 0.24 nm). Further, varying the Mn does not have a large effect on <d>. N is more strongly affected by varying Ni and Mn. At all Ni contents, the alloys with lower bulk Mn show significantly lower N. In addition, increasing the Ni at a constant Mn content (both low and high Mn) shows an increase in N, but this effect is not as significant between the high (≈1.6% Ni) and very high Ni (≈3.5% Ni) steels.

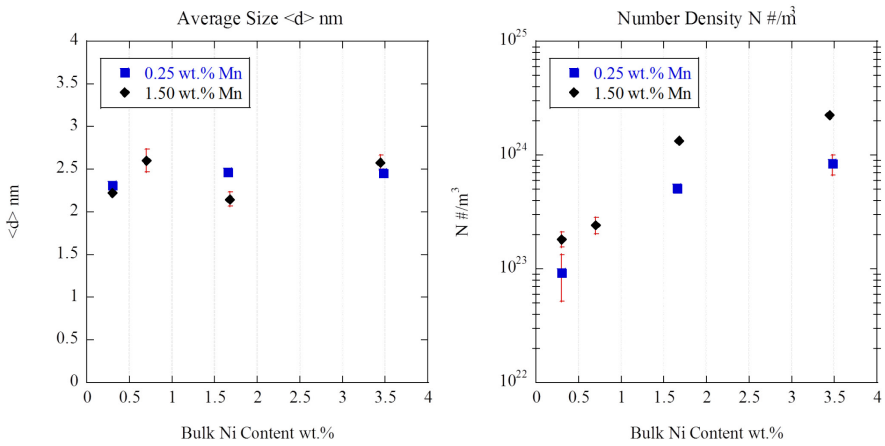

Figure 2.6. The average precipitate <d> (left) and N (right) for 7 steels in the ASM.

As shown in Figure 2.7, similar trends are also observed in plots of f vs the measured bulk Ni content. At low Ni the N and f are very small, and the effect of increasing Mn from 0.24 (R1) to 1.34 (R35) at.% is minimal. For high Mn (green diamonds), the f increases linearly up to ≈ 2.5% at the highest Ni. Finally, at a given Ni content, reduced Mn leads to lower MNSP f, as is further discussed below. Thus, while Ni seems to have the dominant effect in mediating precipitate N and f in low Cu steels, Mn can also has a significant effect at low concentrations.

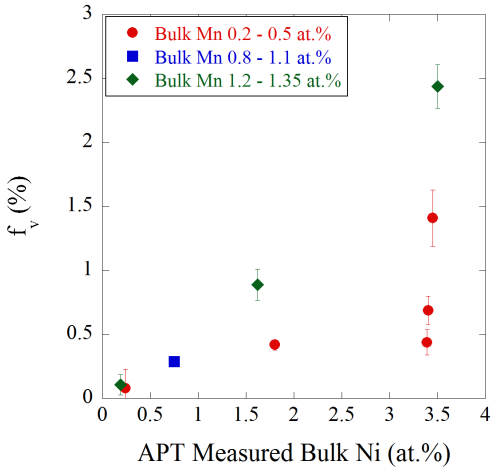

Figure 2.7. APT f vs. bulk Ni (at.%) for the 9 ASM alloys listed in Table 2.4.

2.1.2.2 ASM – Mn Starvation

The previous section demonstrated that high Ni contents lead to higher MNSP f at conventional Mn concentrations, and that this effect is exacerbated at very high Mn. A corollary is that severe embrittlement can be avoided even at high Ni contents if the bulk Mn content is low enough. The ASM matrix is aimed at testing the high-Ni, low-Mn hypothesis, that we call "Mn starvation". Another goal is to develop a better general understanding of the role of Mn (and Si) in steels with a very wide range of Ni contents up to 3.5%.

Figure 2.8 shows the effect of Mn starvation on precipitation. Large MNSP f are avoided by reducing the bulk Mn content of the alloy to 0.25%. Preliminary APT of two high Ni content steels showed a large difference in the precipitate volume fraction for a low Mn of 0.25% (f = 0.65% averaging 4 tips) and high Mn of 1.5% (f = 2.44% averaging 2 tips) alloys. This is also seen in Figure 2.9, plotting f vs the measured bulk Mn content for the 3.5% Ni ASM alloys, showing an almost linear trend.

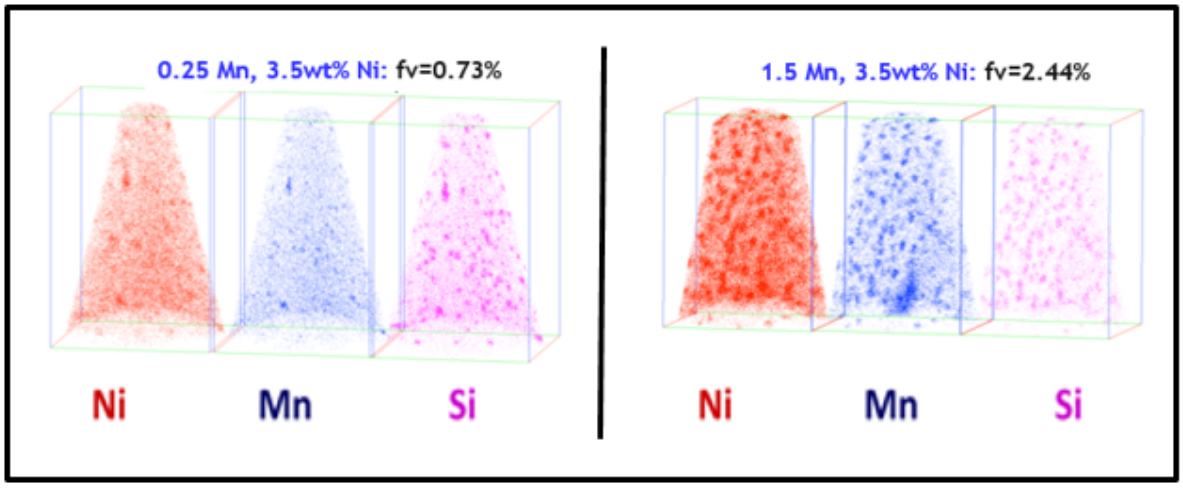

Figure 2.8. Solute maps for the ASM high Ni (3.5wt%) steels with low Mn (left, 0.25wt.%) and high Mn (right, 1.50wt.%).

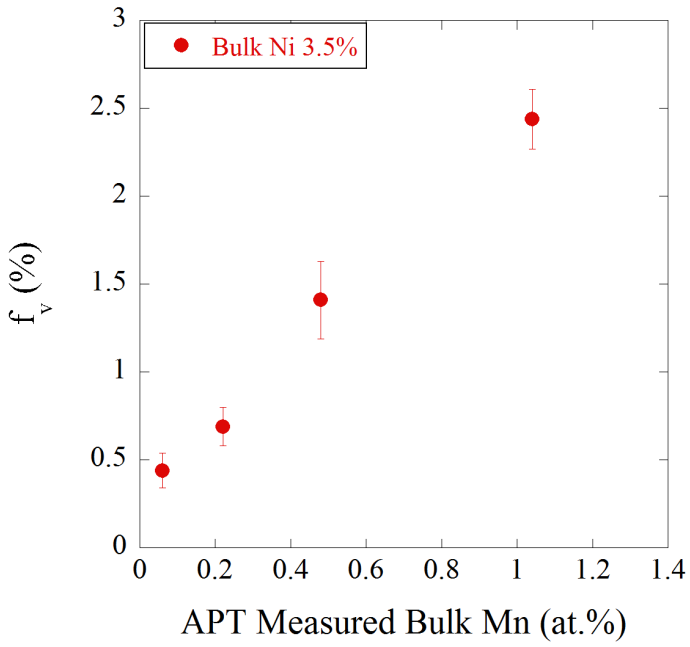

Figure 2.9. The APT f vs. the bulk Mn for the very high 3.5Ni, low Cu ASM steels.

Normal phase selection in typical RPV compositions results in approximately one (Mn + Si) atom for every precipitated Ni atom, since their compositions fall near the observed G or Γ_2 phases, which contain ≈ 50% Ni with the balance composed of Mn and Si. However at the high Ni content of 3.5 wt.%, there may not be enough Mn and Si to reach a ≈ 1/1 Ni/(Mn+Si) ratio, so as to precipitate the maximum Ni from solution. Figure 2.9 plots the observed MNSP compositions on a Mn-Ni-Si projection of the Fe-Mn-Ni-Si system. The MNSP Ni and Si fractions are much higher and the Mn is significantly reduced in the 0.25% Mn alloy. This low Mn precipitate composition falls close to the γ' Ni_3Si silicide phase, which is also seen in Table 2.3. Likewise lower and higher alloy Si contents result in lower and higher corresponding precipitate enrichment in this element, respectively. Overall, the important point is that MNSP phase selection is clearly determined by the bulk alloy chemistry. Future work will investigate the tradeoff of Mn and Si in MNSPs and what effect Si starvation has on precipitation.

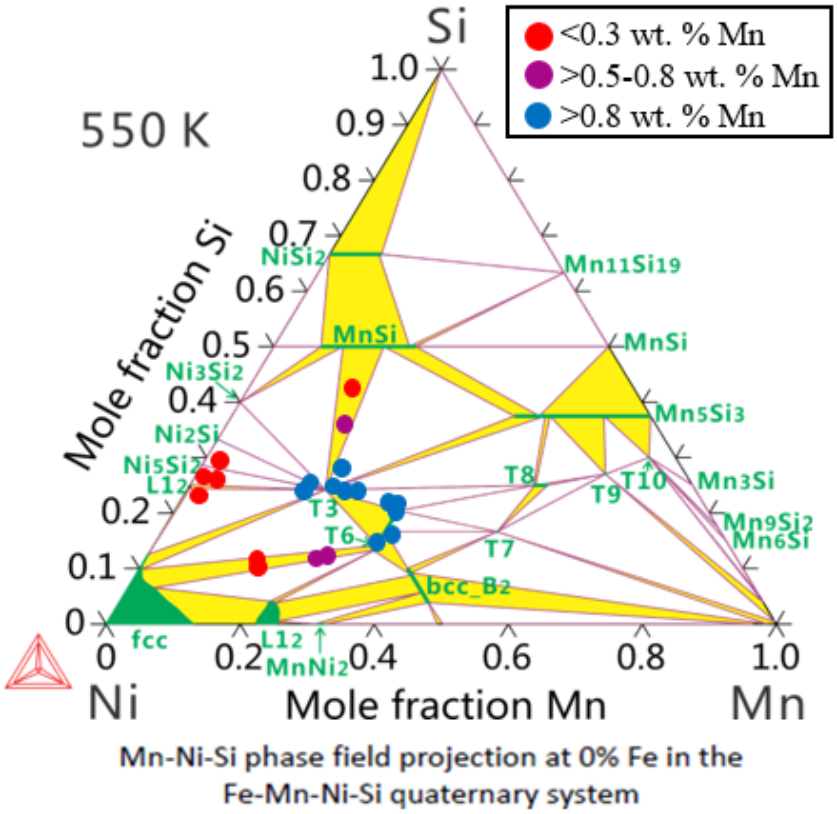

Figure 2.10. APT precipitate compositions for the ASM alloy matrix plotted on the Mn-Ni-Si ternary phase diagram. Each point represents data from a single APT tip.

Figure 2.11 shows that the measured APT f is a linear function of APT measured bulk [2Ni+Cu] for two irradiations. Figure 2.11a plots APT volume fractions from conventional RPV steels, at very high ATR-1 fluence ($1.1x10^{21}$ n/cm^2), believed to be at nearly full phase separation. That is no, or very little, additional precipitation will occur with increasing fluence. Figure 2.11b plots APT volume fraction from the lower fluence ($1.4x10^{20}$ n/cm^2) ATR-2 irradiation over a wider range of solute contents. As expected the lower fluence is associated with less precipitation, which influences the slope of the [2Ni+Cu] fits. The low-Mn alloys have a lower slope. Thus the conventional [2Ni+Cu] chemistry factor does not capture these extremes in composition.

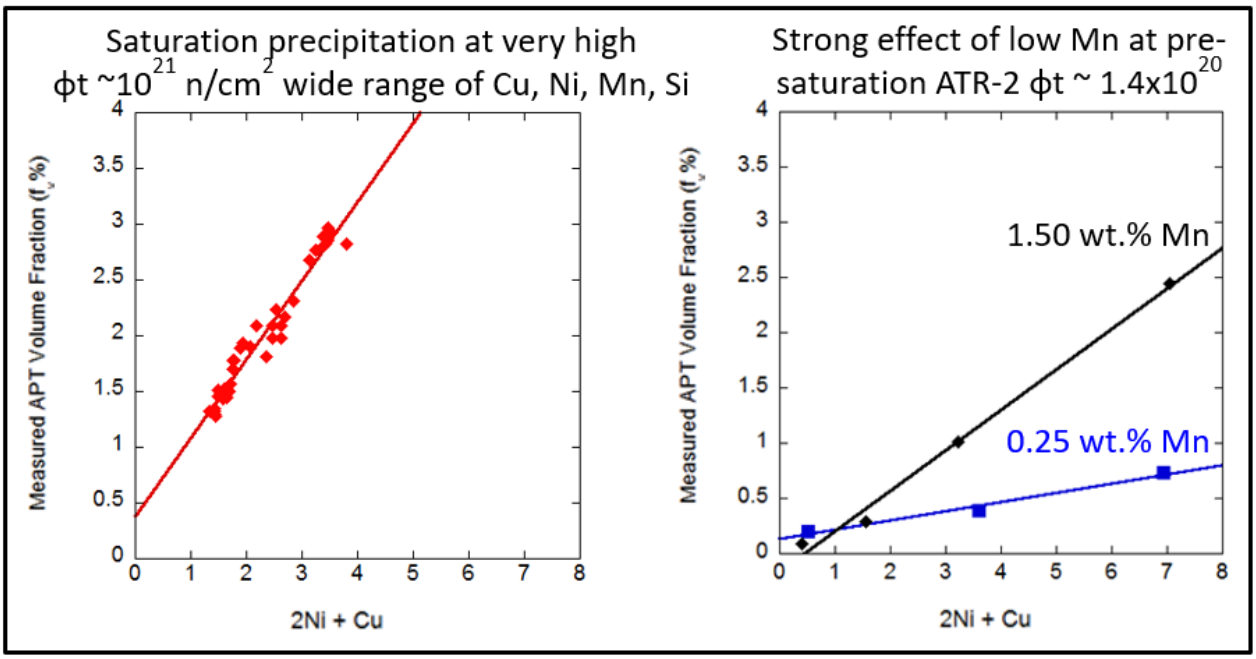

Figure 2.11. APT f as a function of measured bulk 2Ni+Cu from: a) conventional RPV steels at very high ATR-1 fluence condition (1.1x10^{21} n/cm^2); and, b) ASM alloys with two different bulk Mn content (0.25% & 1.50% Mn) from ATR-2, in cup 8 (1.4x10^{20} n/cm^2).

2.2 Small Angle Neutron Scattering

Small angle neutron scattering has been completed on 8 UCSB alloys, 9 surveillance alloys and 20 ASM alloys. These results are shown below. There are compared with measured APT data in a later section and show qualitatively similar results.

2.2.1 UCSB Alloys

Figure 2.12 shows scattering curves for the baseline and irradiated samples for two UCSB alloys, LG (low Cu, medium Ni) on the left and LD (high Cu, high Ni) on the right. Note that the high Cu, high Ni steel has much more scattering from the precipitates, consistent with APT data.

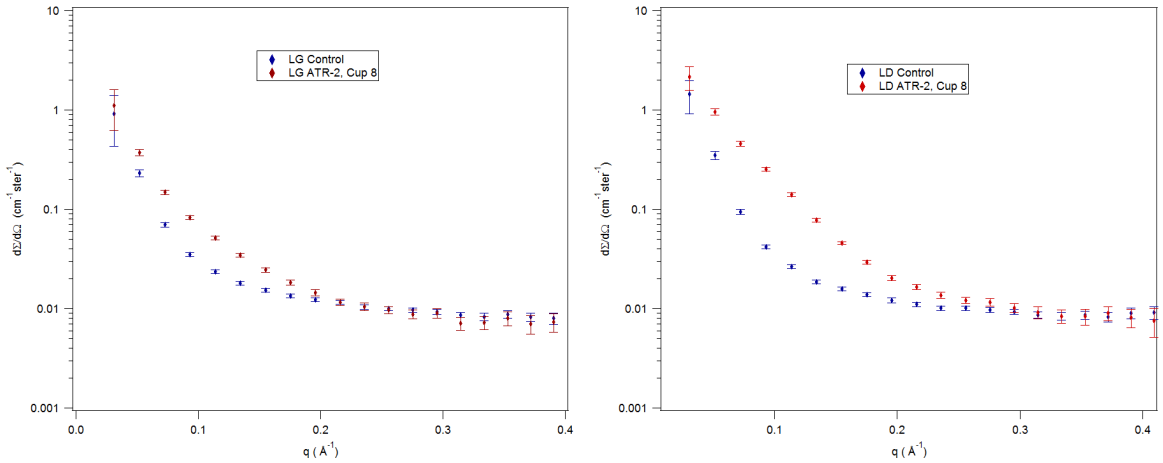

Figure 2.12. SANS 45° scattering curves from an angle on the detector that are higher at intermediate q due to the precipitates. Note that there is less scattering in the irradiated low Cu, medium Ni steel (LG: left) compared to the high Cu, high Ni steel (LD: right).

Table 2.5 shows the SANS measured precipitate <d>, N, f and magnetic-to-nuclear scattering ratios (M/N). The general trends of the effects of Cu and Ni are consistent the APT data. The M/N reflect the composition and atomic density of the precipitates. For example, the measured M/N vary from 1.41 to 2.32 in the UCSB steel matrix. APT shows that the precipitates do not have exact stoichiometric compositions compared to the Γ_2 and G phases. Assuming the APT measured MNSP compositions for LD, the M/N are estimated to be 2.32 and 2.50 for the Γ_2 and G-phases, respectively. These results are preliminary, and the analysis is ongoing. Future work will expand the analysis to the rest of the alloys, and use complementary SAXS data to help to further constrain the compositions and structures precipitates phases.

Table 2.5 Small Angle Neutron Scattering precipitate <d>, N, f, and M/N for the measured UCSB alloys form cup 8.

Alloy	<d> (nm)	+/- (nm)	N (10^{23} m^{-3})	+/- (10^{23} m^{-3})	f (%)	+/- (%)	M/N
C7	2.52	0.13	4.50	1.13	0.37	0.06	1.66
C9	2.96	0.15	1.02	0.26	0.14	0.02	2.35
C13	3.54	0.18	1.00	0.25	0.22	0.03	1.41
C16	4.04	0.20	1.18	0.30	0.40	0.06	2.07
C17	3.64	0.18	3.39	0.85	0.84	0.13	1.60
LD	3.90	0.20	1.79	0.45	0.55	0.08	2.32
LG	3.56	0.18	0.56	0.41	0.13	0.02	2.17
LI	4.20	0.21	0.75	0.19	0.29	0.04	2.27

2.2.2 Surveillance Alloys

Table 2.6 shows SANS data for 9 surveillance alloys. Note that the surveillance M/N are very consistent with the UCSB alloys except in the case of KP, which has the lowest Mn content in both. This is consistent with the high M/N ratio.

Table 2.6 Small Angle Neutron Scattering precipitate <d>, N, f, and M/N for the measured surveillance alloys from cup 8.

Alloy	<d> (nm)	+/- (nm)	N (10^{23} m^{-3})	+/- (10^{23} m^{-3})	f (%)	+/- (%)	M/N
QC1	3.06	0.15	2.81	0.70	0.42	0.06	2.22
D3	2.98	0.15	3.52	0.88	0.49	0.07	2.55
SW1	2.92	0.15	1.79	0.45	0.23	0.03	1.59
SB1	2.88	0.14	3.05	0.76	0.38	0.06	2.13
SB2	2.64	0.13	1.46	0.37	0.14	0.02	14.75
SW2	3.24	0.16	3.66	0.91	0.65	0.10	2.17
SW3	3.48	0.17	2.96	0.74	0.65	0.10	2.58
SW4	2.62	0.13	2.11	0.53	0.2	0.03	2.1
SW5	2.64	0.13	2.17	0.54	0.21	0.03	2.68

2.2.3 ASM

Table 2.7 shows the SANS measured precipitate <d>, N, f and M/N for 20 ASM alloys. The ASM alloys show very large ranges of M/N, and a number of them have M/N >

10 or < 1.5. This is very different than the UCSB and surveillance matrices where most M/N fell between 1.5 and 2.5.

Table 2.7 Small Angle Neutron Scattering precipitate <d>, N, f, and M/N for the measured ASM alloys form cup 8.

Alloy	<d> (nm)	+/-	N (m^{-3})	+/-	f (%)	+/-	M/N
R1	3.84	0.19	1.20E+22	3.00E+21	0.04	0.01	9.96
R4	4.64	0.23	7.58E+21	1.90E+21	0.04	0.01	10.87
R10	2.24	0.11	3.00E+24	7.50E+23	1.77	0.27	1.78
R14	3.86	0.19	4.50E+23	1.13E+23	1.35	0.20	1.17
R17	2.28	0.11	2.90E+24	7.25E+23	1.82	0.27	1.69
R18	2.70	0.14	2.25E+24	5.63E+23	2.31	0.35	1.93
R20	2.28	0.11	3.00E+23	7.50E+22	0.19	0.03	10.68
R21	2.92	0.15	1.10E+23	2.75E+22	0.15	0.02	15.22
R22	2.22	0.11	9.40E+23	2.35E+23	0.54	0.08	1.54
R26	2.26	0.11	6.30E+23	1.58E+23	0.39	0.06	19.3
R28	2.52	0.13	6.30E+23	1.58E+23	0.53	0.08	22.9
R32	1.49	0.07	1.25E+24	3.13E+23	1.72	0.26	1.31
R33	2.20	0.11	5.70E+23	1.43E+23	0.32	0.05	13.6
R34	3.04	0.15	9.10E+22	2.28E+22	0.13	0.02	> 100
R35	2.22	0.11	1.21E+23	3.03E+22	0.09	0.01	0.98
R37	2.50	0.13	7.70E+22	1.93E+22	0.06	0.01	1.36
R39	2.58	0.13	1.39E+23	3.48E+22	0.13	0.02	1.65
R42	1.74	0.09	1.74E+24	4.35E+23	0.49	0.07	3
R47	1.78	0.09	1.10E+24	2.75E+23	0.32	0.05	3.44
R48	2.16	0.11	1.50E+24	3.75E+23	0.81	0.12	2.8

The large variation of M/N ratios is due to the wide range of compositions in the ASM, hence, corresponding differences in precipitate compositions and phases (see Figure 2.10). For example, as noted previously, the precipitates in R34 and R26 have compositions of approximately Ni_3Si, while in SANS they have M/N of 19.3 and > 100, respectively. The scattering length of the Ni_3Si precipitates similar to that of the Fe matrix, so the corresponding scattering contrast is small, leading to very large M/N assuming these features are not magnetic. The two unknowns are the actual phase and corresponding atomic density and the magnetization of the precipitate, if any.

2.3 *Automated SPT*

Automated SPT was completed on the full baseline matrix of ASM alloys, along with the 48 ASM alloys from cup 8 currently at UCSB.

2.3.1 *Baseline Testing*

Before testing the irradiated samples from the ATR-2 experiment, the automated SPT instrument required qualification and calibration, including establishing the "optimal" offset for defining the shear yield stress (τ_y). As shown in

Figure 2.13, the calibration was carried out on the entire ASM baseline matrix by determining automated SPT τ_y at various offsets compared to the corresponding τ_y from the manual tester, which used a 0.2% offset. Figure 2.13a-d show the results for automated SPT offsets of a) 0.2%, b) 0.4%, c) 0.6% and d) 0.9%, respectively. An automated SPT offset of 0.9% provides the best agreement, so it was used to determine τ_y for the baseline. The reason that the offsets differ is corresponding differences in the loading compliance in the two cases.

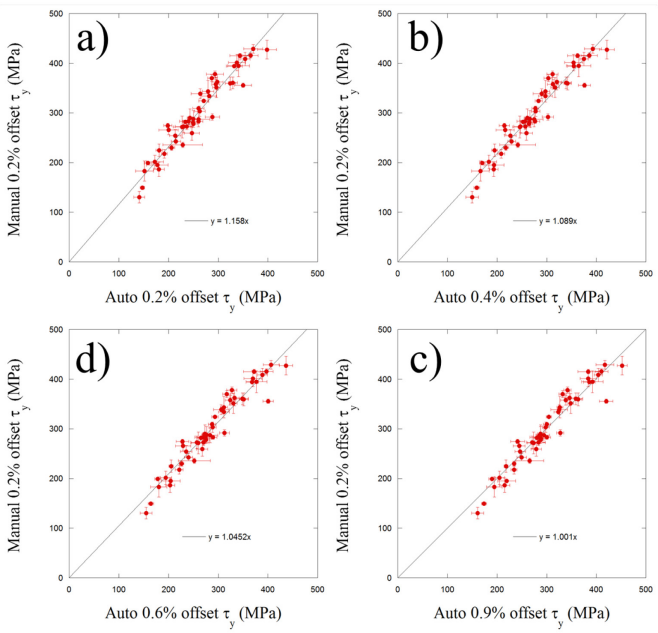

Figure 2.13. Manual vs. automated τ_y for various automated SPT offsets.

Figure 2.14 shows the tensile σ_y vs. the automated SPT measured τ_y using a 0.9% offset. The linear least square fit slope is 1.78 that is, as expected, similar to the original τ_y vs. σ_y relation for the manual SPT of 1.77 [6]. Note that there are two outliers, R24 and R46, which will be retested.

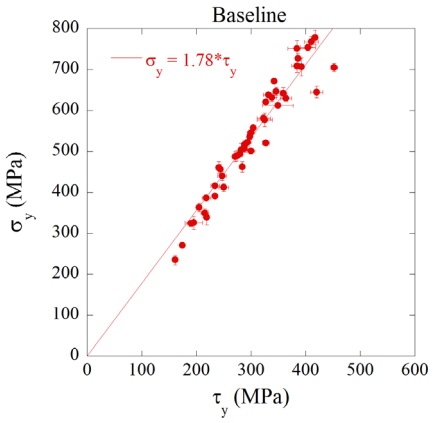

Figure 2.14. Baseline tensile σ_y vs. SPT τ_y for the ASM alloys.

Figure 2.15 shows an almost 1:1 agreement between the S_{max} for the manual and automated SPT measurements. However, the 2 outliers also persist in these cases.

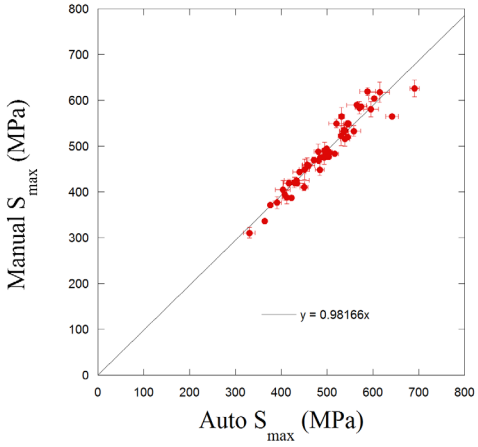

Figure 2.15. Measured manual vs. automated SPT S_{max}.

2.3.2 ATR-2, Cup 8 Testing

Automated SPT was completed on all ASM irradiated alloys currently at UCSB. The baseline and irradiated τ_y (using an offset of 0.9%) and S_{max} are shown in Table 2.8.

Table 2.8 τ_y and S_{max} from the automated SPT instrument for all ASM alloys at UCSB from cup 8 in the baseline and irradiated conditions.

Alloy	$\tau_{y,u}$ (MPa)	±	$\tau_{y,I}$ (MPa)	±	$S_{max,U}$ (MPa)	±	$S_{max,I}$ (MPa)	±
R1	215	10	257	9	412	8	475	16
R2	174	5	202	9	364	10	410	13
R3	161	12	173	12	330	3	380	8
R4	219	18	257	11	434	4	508	11
R5	190	7	226	6	376	6	479	7
R6	218	4	288	13	407	4	535	10
R8	195	16	260	11	403	11	497	14
R9	234	6	348	8	430	10	593	3
R10	410	13	609	23	603	13	831	9
R11	338	10	578	8	537	8	766	16
R12	300	7	551	8	481	6	740	13
R13	392	22	602	17	615	19	802	17
R14	364	7	561	5	537	4	790	30
R15	386	12	596	23	574	27	815	23
R16	384	21	643	10	564	6	844	17
R17	404	8	590	19	570	11	818	25
R18	417	18	634	10	588	17	808	40
R20	205	10	296	12	391	6	544	31
R21	241	14	351	14	439	4	571	6
R22	323	9	474	13	536	4	718	11
R23	247	11	421	4	428	7	654	8
R24	420	14	443	13	641	26	713	5
R25	284	13	407	29	459	21	625	14
R26	349	6	436	12	531	11	651	18
R27	244	12	321	13	417	8	517	5
R28	325	17	423	28	520	22	650	11
R29	274	13	405	20	450	9	618	15
R30	282	16	297	4	471	30	546	9
R31	359	14	460	11	559	41	711	10
R32	384	16	612	17	595	7	820	17
R33	288	9	381	19	481	33	585	6
R34	294	11	332	8	494	13	554	19
R35	288	7	313	5	503	11	573	12
R36	234	4	266	11	422	4	477	9
R37	327	7	353	8	544	21	575	15
R38	250	10	271	8	450	11	496	8
R39	271	12	315	7	484	3	552	10
R40	288	10	324	10	517	7	583	18
R41	280	6	355	12	485	7	588	10
R42	298	7	340	6	496	4	587	9
R43	300	7	339	15	504	7	575	26
R44	304	5	373	14	499	8	613	22
R45	346	10	338	28	539	16	585	13
R46	452	10	629	4	691	8	821	13
R47	288	6	369	8	494	15	583	4
R48	332	7	490	9	545	13	711	5
R49	327	6	405	15	530	8	625	13
R50	342	7	433	7	545	13	697	15

In addition to ASM alloys, SPT were varied out on a number of UCSB alloys in the irradiated condition. Baseline testing on this matrix is currently ongoing, so they are not listed in the table above. Figure 2.16 plots the tensile measured σ_y vs the automated SPT measured τ_y. Interestingly, while this correlation also shows a linear correlation between the σ_y and τ_y, with a slope ≈ 2.06%. We are currently investigating why the irradiated samples show a different correlation between σ_y and τ_y than the unirradiated baseline samples, but we hypothesize that this difference is caused by corresponding differences in strain hardening in the irradiated versus unirradiated condition. Work on the σ_y and τ_y correlations is ongoing, primarily based on finite element modeling.

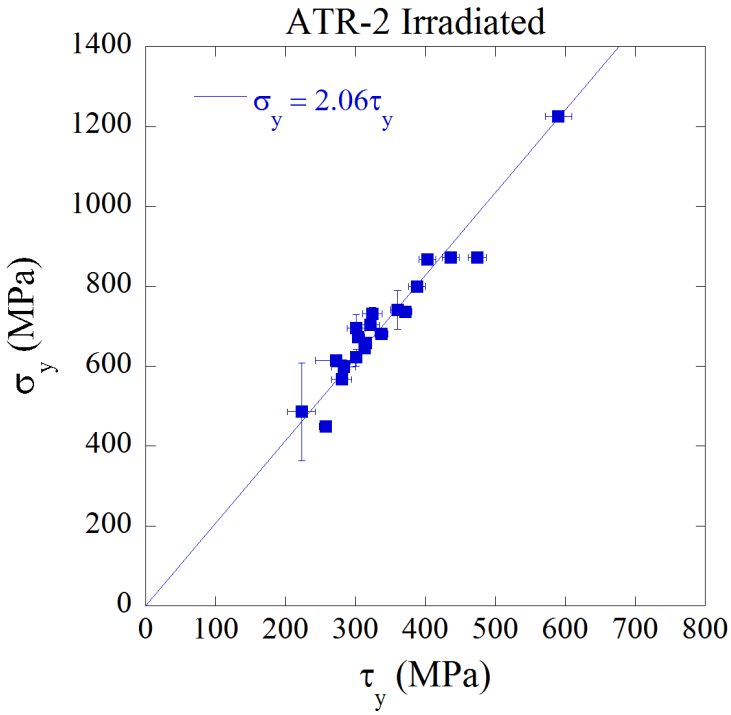

Figure 2.16. σ_y vs. τ_y for irradiated alloys from cup 8.

2.4 Microhardness

Vickers microhardness was also completed on all ASM alloys currently at UCSB. This data, along with the converted $\Delta\sigma_y$, which was calculated as $\Delta\sigma_y = 3.33*\Delta\mu H$, is given in Table 2.9.

Table 2.9 Microhardness data for ASM alloys tested at UCSB. The change in Vickers hardness due to irradiation at the ATR-2 condition was converted to shifts in yield stress.

Alloy	μH_{BL} (kg/mm^2)	±	μH_{Irr} (kg/mm^2)	±	$\Delta\sigma y$ (MPa)	±
R1	160.7	1.8	175.9	4.0	50.7	14.4
R2	144.0	2.0	181.5	2.4	124.7	10.4
R3	150.5	2.7	188.1	4.0	125.3	15.9
R4	175.3	3.1	205.1	4.8	99.3	19.0
R5	149.9	1.9	161.1	1.8	37.2	8.7
R6	170.4	2.9	233.8	7.6	211.1	27.2
R7*	187.0	2.5				
R8	173.6	2.9	224.6	3.0	169.8	14.0
R9	172.8	1.9	282.4	3.3	365.0	12.6
R10	290.8	3.9	422.9	7.8	440.1	29.2
R11	250.3	4.6	424.6	5.9	580.6	25.0
R12	235.3	2.0	403.2	4.6	559.2	16.6
R13	289.8	1.4	436.0	6.2	486.7	21.3
R14	249.7	3.3	429.0	2.9	597.1	14.6
R15	284.2	1.4	461.3	2.1	589.6	8.4
R16	282.7	1.7	443.1	4.5	534.1	15.9
R17	298.0	2.7	426.5	2.8	427.7	13.1
R18	292.7	2.1	439.7	4.4	489.5	16.1
R19*	222.5	3.0				
R20	178.6	5.9	239.5	4.6	203.1	25.0
R21	201.1	2.2	285.2	5.4	279.9	19.4
R22	253.3	2.7	351.3	3.9	326.1	15.7
R23	202.4	2.5	332.1	5.6	431.8	20.5
R24	286.0	3.1	318.2	11.0	107.1	38.0
R25	223.5	4.0	322.3	4.0	329.1	18.8
R26	253.8	4.0	336.4	4.1	275.1	18.9
R27	206.4	5.3	275.6	2.2	230.5	18.9
R28	269.7	5.4	346.0	4.6	254.2	23.8
R29	230.8	3.8	304.6	5.7	245.8	22.8
R30	208.2	6.1	258.4	4.6	167.2	25.6
R31	287.5	5.7	360.1	5.2	241.6	25.7
R32	266.1	4.0	459.8	1.8	644.9	14.7
R33	234.7	3.2	277.4	4.2	142.1	17.6
R34	237.5	3.8	287.1	2.8	165.1	15.6
R35	238.9	3.2	274.1	3.8	117.2	16.6
R36	184.8	7.4	224.8	2.3	133.4	25.7
R37	264.3	2.7	276.4	3.7	40.3	15.4
R38	208.7	5.1	234.1	4.0	84.8	21.5
R39	217.6	4.4	258.3	4.3	135.5	20.6
R40	223.0	5.1	271.3	2.9	161.0	19.6
R41	237.0	2.8	301.5	3.8	214.9	15.6
R42	221.8	5.1	293.8	5.8	239.6	25.8
R43	239.1	3.5	287.0	4.5	159.6	19.1
R44	235.3	3.1	295.6	5.8	201.1	22.0
R45	258.7	1.7	299.6	3.6	136.0	13.2
R46	306.0	6.7	476.8	2.6	568.5	23.9
R47	229.8	4.0	296.6	9.7	222.4	34.9
R48	295.6	6.6	357.0	7.5	204.4	33.3
R49	242.7	2.7	328.1	3.8	284.4	15.4
R50	272.9	3.9	353.6	3.1	268.4	16.7

**Irradiated samples not yet at UCSB*

3. Conclusions and Future Work

3.1 Conclusions

The ATR-2 experiment will generate a huge database on both microstructure and mechanical property data for a large number of RPV steels with a wide range of alloy compositions for different irradiation conditions. This report gives a brief overview of the ATR-2 PIE data taken over the past 9 months. While a major focus of upcoming work is to continue testing and characterization of additional irradiated alloys, especially those from lower temperature cups, future work will expand the analysis of both current and new data, developing correlations between the measurables derived from the various techniques.

3.2 Updated Testing Plan

UCSB is currently awaiting for what is likely to be the final shipment of irradiated alloys from cups 7 and 8. We will finish irradiated SPT on the highest priority alloys in these high fluence cups and save small discs for future mechanical property testing and microstructural characterization. In addition, we are in the process of completing baseline SPT on the remaining alloys in the ATR-2 irradiation. Once these tasks are completed, targeted to be within the next few months, the focus of testing will move to the two lower temperature (250 and 270°C) ATR-2 conditions at fluences of $\approx 1.2 \times 10^{20}$ n/cm^2.

4. References

1. Odette GR, Yamamoto T, Wells PB, Almirall N, et al. "Update on the ATR-2 Reactor Pressure Vessel Steel High Fluence Irradiation Project," 2016; UCSB ATR-2 2016-1.
2. "As-Run Thermal Analysis of the UCSB-2 Experiment in the ATR," 2016; ATR NSUF ECAR No. 3218, Project No. 30946.
3. "As-Run Physics Analysis for hte UCSB-2 Leadout Experiment in I-22," 2016; ATR NSUF ECAR No. 3219, Project No. 30946.
4. Eason ED, Odette GR, Nanstad RK and Yamamoto T. "A physically based correlation of irradiation-induced transition temperature shifts for RPV steels," Oak Ridge

National Lab, 2007; ORNL/TM-2006/530.

5. Wells PB, Yamamoto T, Miller B, Milot T, et al. "Evolution of manganese–nickel–silicon-dominated phases in highly irradiated reactor pressure vessel steels", *Acta Mater.* 2014;80:205–219.
6. Milot TS. "Establishing Correlations for Predicting Tensile Properties Based on the Shear Punch Test and Vickers Microhardness Data" [PhD Thesis]. University of California, Santa Barbara, 2013.